


RESEARCH ARTICLE

Seasonality of spectral radiative fluxes and optical properties of Arctic sea ice during the spring–summer transition

Ran Tao^{1,2,*} , Marcel Nicolaus¹, Christian Katlein¹, Philipp Anhaus¹, Mario Hoppmann¹, Gunnar Spreen², Hannah Niehaus², Evelyn Jäkel³, Manfred Wendisch³, and Christian Haas^{1,2}

The reflection, absorption, and transmittance of shortwave solar radiation by sea ice play crucial roles in physical and biological processes in the ice-covered Arctic Ocean and atmosphere. These sea-ice optical properties, particularly during the melt season, significantly impact energy fluxes within and the total energy budget of the coupled atmosphere-ice-ocean system. We analyzed data from autonomous drifting stations to investigate the seasonal evolution of the spectral albedo, transmittance, and absorptivity for different sea-ice, snow, and surface conditions measured during the MOSAiC expedition in 2019–2020. The spatial variability of these properties was small during spring and increased strongly after melt onset on May 26, 2020, when liquid water content on the surface increased, largely accounting for the enhanced variability. The temporal evolution of surface albedo and sea-ice transmittance was mostly event-driven, thus containing episodic elements. Melt ponds reduced the local surface albedo by 31%–45%. Over the melting season, single ponding events increased the energy deposition of the sea ice by 35% compared to adjacent bare ice. Thus, single melt ponds may impact the summer energy budget as much as seasonal evolution over 1 month. Absorptivity and transmittance showed strong temporal and spatial variabilities independently of surface conditions, possibly due to the different internal sea-ice properties and under-ice biological processes. The differences in seasonal evolution shown for different sea-ice conditions strongly impacted the partitioning of shortwave solar radiation. This study shows that the formation and development of melt ponds, in reducing albedo by a third of bare ice sites, can notably increase the total summer heat deposition. The vastly different seasonal evolutions, different sea-ice conditions, and timing and duration of ponding events need to be considered when comparing local in-situ observations with large-scale satellite remote sensing datasets, which we suggest can help to improve numerical models.

Keywords: Arctic sea ice, Optical property, Radiative fluxes, Albedo and transmittance

1. Introduction

The surface energy budget of the summer Arctic sea-ice cover is affected significantly by the observed decline of sea ice (e.g., Comiso, 2012; Nicolaus et al., 2012). The Arctic sea ice shows an earlier melt onset and later freeze-up, and thus a longer melt season. Sea-ice extent is shrinking (Stroeve et al., 2014; Serreze and Stroeve, 2015), thickness is decreasing (e.g., Haas et al., 2008; Kwok, 2018), and multi-year ice (MYI) is largely replaced

by seasonal first-year ice (FYI; e.g., Maslanik et al., 2011; Stroeve and Notz, 2018). Concurrently, the near-surface air temperature in the Arctic has increased 2–3 times more than the corresponding global mean surface temperature (e.g., Wendisch et al., 2023). The increasing air temperature provides more heat to melt the snow cover, resulting in decreasing albedo (Nicolaus et al., 2010a; Perovich and Polashenski, 2012). In particular, the transition from dry to wet snow results in a significant albedo decrease (Nicolaus et al., 2010a; Perovich and Polashenski, 2012). The lower sea-ice albedo during this period results in more solar radiative energy being absorbed by the sea ice and the ocean underneath (e.g., Comiso, 2012; Serreze and Stroeve, 2015; Stroeve and Notz, 2018). The spatial and temporal variability of surface properties such as albedo, transmittance, and absorptivity increase after melt onset and subsequent melt pond formation (e.g., Perovich and Elder, 2002).

¹ Alfred-Wegener-Institut Helmholtz-Zentrum für Polar- und Meeresforschung, Bremerhaven, Germany

² Institute of Environmental Physics, University of Bremen, Bremen, Germany

³ Leipzig Institute for Meteorology, Leipzig University, Leipzig, Germany

* Corresponding author:
Email: ran.tao@awi.de

The melting snow increases the transmittance of the snow-covered sea ice and, as a result, increases the penetration of downward solar irradiance through the sea ice, which impacts physical and biological processes underneath the sea-ice cover (e.g., Perovich et al., 2008; Perovich and Richter-Menge, 2015; Katlein et al., 2019; Ardyna et al., 2020). On the aggregate scale, approximately 8% of the incident solar irradiance is transmitted into the ocean below in 1 year (Perovich, 2005). The overwhelming amount (approximately 96%) of the annually transmitted solar radiative energy penetrates through the sea-ice layer during the 4-month period from May to August when a sufficient amount of irradiance can be deposited on the surface with low albedo (Perovich, 2005; Arndt and Nicolaus, 2014).

A detailed investigation of the temporal evolution and spatial variability of the surface and optical properties is needed to accurately represent the large-scale energy balance of the Arctic sea ice. Here, we present a dataset of spectral albedo and transmittance from 10 autonomous radiation measurement stations deployed during the Multidisciplinary Drifting Observatory for the Study of Arctic Climate (MOSAIC) expedition in 2019–2020 (Nicolaus et al., 2022). In-situ observations provide detailed insight into the radiative partitioning in and through sea ice, which is otherwise inaccessible via satellite observation. We focus on the period from April 1 to July 18, 2020, when the Arctic sea ice transitioned from spring to summer. Our analysis identifies the seasonality and key events during this transition, examines the radiative partitioning during the transition period, and highlights their impact on the larger-scale energy balance.

2. Methods

2.1. The MOSAIC drift

The dataset presented in this study was obtained during the MOSAIC expedition (2019–2020) with the German research icebreaker *Polarstern* (Knust, 2017), following the Transpolar Drift (Nicolaus et al., 2022). The drift of *Polarstern* consisted of three phases:

- (1) Drift 1 started in the central Arctic at 85°N on October 4, 2019, and lasted until May 16, 2020, when *Polarstern* left the floe and paused the manned observation, while autonomous measurements continued.
- (2) Drift 2 started on the same floe as Drift 1 on June 19, 2020, and lasted until July 31, 2020, when the floe disintegrated in Fram Strait (78.9°N). Subsequently,
- (3) Drift 3 started on a new floe near the North Pole (87.7°N) on August 21, 2020, and followed the Transpolar Drift stream until September 20, 2020.

Altogether 10 autonomous stations were deployed during the MOSAIC expedition to measure spectral solar radiation fluxes above and below the sea ice (**Table 1**). **Figure 1** shows the drift track of the 10 radiation stations, which followed the concept described by Nicolaus et al. (2010b). The majority (7) of the radiation stations were

installed during Drift 1 from October 5, 2019, to August 8, 2020, when the autonomous stations were recovered. The data collected during this period provide important observations covering the key spring–summer transition from May 16 to June 19, 2020, when no manned observations were possible due to the absence of *Polarstern* (between Drifts 1 and 2). Furthermore, autonomous buoys 2020M29 and 2019S94 provide the evolution of air and surface temperature during the melt season.

2.2. Radiation station measurements and data processing

Each radiation station consisted of three RAMSES-ACC-VIS hyperspectral radiometers (TriOS GmbH, Rastede, Germany; Nicolaus et al., 2010b), measuring spectral irradiance from 320 nm to 950 nm with a spectral resolution of 3.3 nm. Measurement interval was 10 minutes. **Figure 2** shows photos of both the above-ice and under-ice sensors. Above the ice, the upward-looking sensor measured incident (downwelling) irradiance, $E_i(\lambda, \tau)$, and the downward-looking sensor measured reflected (upwelling) irradiance, $E_u(\lambda, \tau)$. The sensor installed under the ice measured the transmitted (downwelling) irradiance, $E_d(\lambda, \tau)$. The under-ice sensor was placed approximately 0.5 m below the ice bottom at the deployment date, measuring the transmitted irradiance through the sea ice, which can be covered with snow, the surface scattering layer (bare ice), or liquid water (melt pond). During the observation time, the distance from the under-ice sensor to the ice bottom varied due to sea ice growth/melt.

The spectral irradiance above (downwelling, $E_i(\lambda, \tau)$, and upwelling, $E_u(\lambda, \tau)$) and below (downwelling, $E_d(\lambda, \tau)$) the sea ice layer was recorded in counts per channel and then calibrated to absolute spectral irradiances (in $\text{W m}^{-2} \text{nm}^{-1}$) based on individual calibration files for each sensor (Nicolaus et al., 2010b). The spectra were interpolated onto a 1 nm grid to calculate the ratios of spectral albedo, $\alpha(\lambda, \tau)$:

$$\alpha(\lambda, \tau) = E_u(\lambda, \tau) / E_i(\lambda, \tau) \quad (1)$$

and transmittance, $\tau(\lambda, \tau)$, as a ratio of E_d to E_i :

$$\tau(\lambda, \tau) = E_d(\lambda, \tau) / E_i(\lambda, \tau) \quad (2)$$

as a function of wavelength (λ) and time (t).

Nicolaus et al. (2010b) found insufficient data quality between 748 nm and 773 nm with oxygen absorption around 760 nm, as the irradiance was sampled at slightly different wavelength due to the different wavelength grids of the two above-ice sensors. Hence, the albedo was interpolated linearly within this wavelength range.

The wavelength-integrated broadband albedo, $\alpha_T(t)$, and transmittance, $\tau_T(t)$, were calculated within the wavelength range of 350 nm to 920 nm via the following equations:

$$\alpha_T(t) = \frac{\int \alpha(\lambda, t) E_i(\lambda, t) d\lambda}{\int E_i(\lambda, t) d\lambda} \quad (3)$$

$$\tau_T(t) = \frac{\int \tau(\lambda, t) E_i(\lambda, t) d\lambda}{\int E_i(\lambda, t) d\lambda} \quad (4)$$

Table 1. Operational times and metadata of the autonomous radiation stations operated during the MOSAiC expedition

Station Name	Site	Initial Snow Depth (m)	Initial Ice Thickness (m)	Deployment	First Good Data	Last Good Data	Failure/ Recovery	Comment
2019R8	L1	0.18	0.78	October 05, 2019	October 6, 2019	June 13, 2020	August 06, 2020	Low sun elevation angle, hardware malfunction
2019R9	L2	0.10	0.30	October 07, 2019	March 13, 2020	June 12, 2020	June 17, 2020	Data interruption due to hardware malfunction
2020R10	CO1	0.07	1.49	March 08, 2020	March 13, 2021	July 20, 2020	July 21, 2020	Destroyed by ridge activity
2020R11	LM^a	0.18	1.59	March 26, 2020	March 29, 2020	July 18, 2020	August 01, 2020	Long-term data during the spring–summer transition
2020R12	L3^a	0.08	1.67	April 24, 2020	April 24, 2020	July 22, 2020	August 08, 2020	Long-term data during the spring–summer transition
2020R13	CO1	0.92	4.28	May 06, 2020	May 6, 2020	May 12, 2020	May 15, 2020	Destroyed by ridge activity
2020R14	CO1^a	0.12	3.13	April 03, 2020	April 03, 2020	July 15, 2020	July 15, 2020	Long-term data during the spring–summer transition
2020R15	CO2	0.01	1.52	July 12, 2020	July 13, 2020	July 19, 2020	July 19, 2020	Data interruption due to hardware malfunction
2020R21	CO3	0.35 (pond depth)	0.59	August 27, 2020	August 27, 2020	September 25, 2020	November 14, 2020	Deployed in a melt pond
2020R22	CO3	Unknown	1.34	August 21, 2020	August 21, 2020	September 12, 2020	September 12, 2020	Data interruption due to hardware malfunction

^aThe three radiation stations discussed in detail in the text are in bold (2020R11 at site LM, 2020R12 at site L3, and 2020R14 at site CO1); station 2020R14 at site CO1 is referred to as site CO.

The wavelength-integrated irradiances, $E_i(t)$, $E_d(t)$, $E_u(t)$, were integrated within the wavelength range of 350 nm to 920 nm. The radiative fluxes of sea ice were calculated:

(i) Net irradiance entering the sea ice, E_{ice} ($E_i \cdot (1 - \alpha_T(\tau))$; Equation 3),

$$E_{ice}(t) = E_i(t) - E_u(t) \quad (5)$$

(ii) Irradiance absorbed by the sea ice layer, E_a , and absorptivity, $\text{abs}_T(t)$:

$$E_a(t) = E_i(t) - E_u(t) - E_d(t) \quad (6)$$

$$\text{abs}_T(t) = 1 - \alpha_T(t) - \tau_T(t) \quad (7)$$

The upward irradiance from the ocean to the sea-ice bottom was omitted from the calculation as it may be

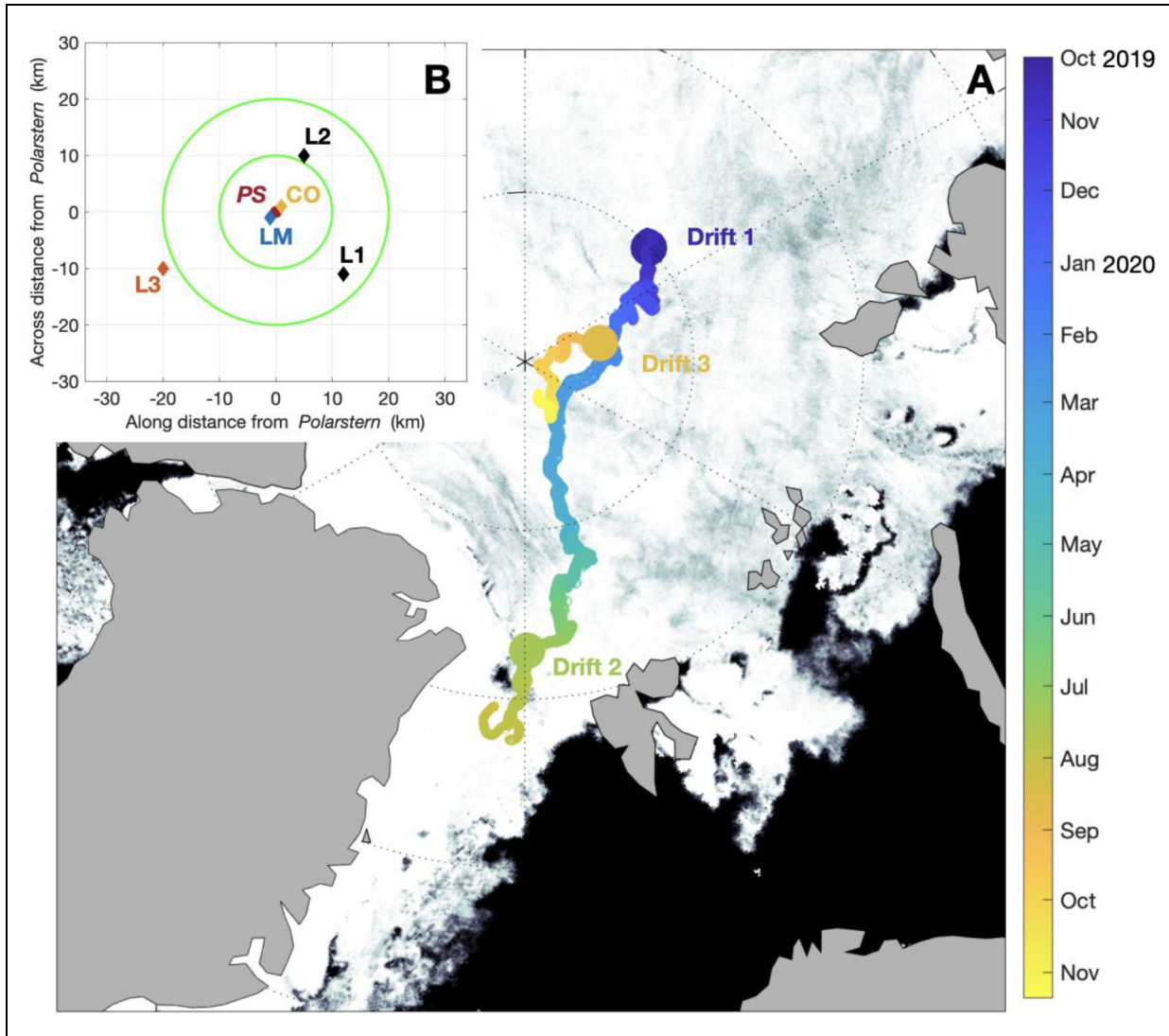


Figure 1. Drift tracks, distribution of sites, and sea-ice concentration during the MOSAiC expedition. (A) Drift tracks of the radiation stations from October 2019 to November 2020. The starting point of Drifts 1, 2, and 3 are labeled accordingly. The background shows the sea-ice concentration retrieved via Advanced Microwave Scanning Radiometer 2 (AMSR2) on May 25, 2020. (B) Relative positions of the Distributed Network sites (L1, L2, L3, LM) at the beginning of Drift 1, centered around *Polarstern* (PS) and the Central Observatory (CO).

assumed to be extremely small (approximately 1%; Smith and Baker, 1981).

- (iii) Sea ice melt rate (internal m_{eqi} and bottom m_{eqo}) from the accumulated absorbed irradiance E_a (i.e., $1 - \text{albedo}$; Equation 3) and transmitted irradiance E_d over time through the surface and the ice:

$$m_{eqi} = \frac{Q_A}{L_{melt} \cdot \rho_{ice}} \quad (8)$$

$$m_{eqo} = \frac{Q_E}{L_{melt} \cdot \rho_{ice}} \quad (9)$$

where Q_A is the absorbed irradiance E_a accumulated over time: $Q_A = \sum E_a \Delta t$; and the transmitted irradiance E_d accumulated over time: $Q_E = \sum E_d \Delta t$, both assuming sea ice has a density $\rho_{ice} = 917 \text{ kg m}^{-3}$, and a latent heat of melt $L_{melt} = 0.3335 \text{ J kg}^{-1}$.

- (iv) Albedo ratio ($\alpha_{900}/\alpha_{500}$) between the albedo at 900 nm (α_{900}) and the albedo at 500 nm (α_{500}). This ratio is sensitive to the liquid water content at the surface, and thus an indicator of ponding, due to high absorption of water at 900 nm compared to 500 nm. The albedo ratio decreases as water accumulates at the surface.
- (v) Transmittance ratio (τ_{600}/τ_{450}) between transmittance at 600 nm (τ_{600}) and transmittance at 450 nm (τ_{450}). This ratio is sensitive to the Chlorophyll-a content of the ice and upper ocean, and an increase may be used as an indicator for biological activities in or directly underneath sea ice (e.g., Perovich et al., 1993; Ehn et al., 2008).
- (vi) We derived the wavelength of maximum transmittance of each spectrum as an indicator for the spectral shape that may be associated with biological influences, as used in Nicolaus et al. (2010a).

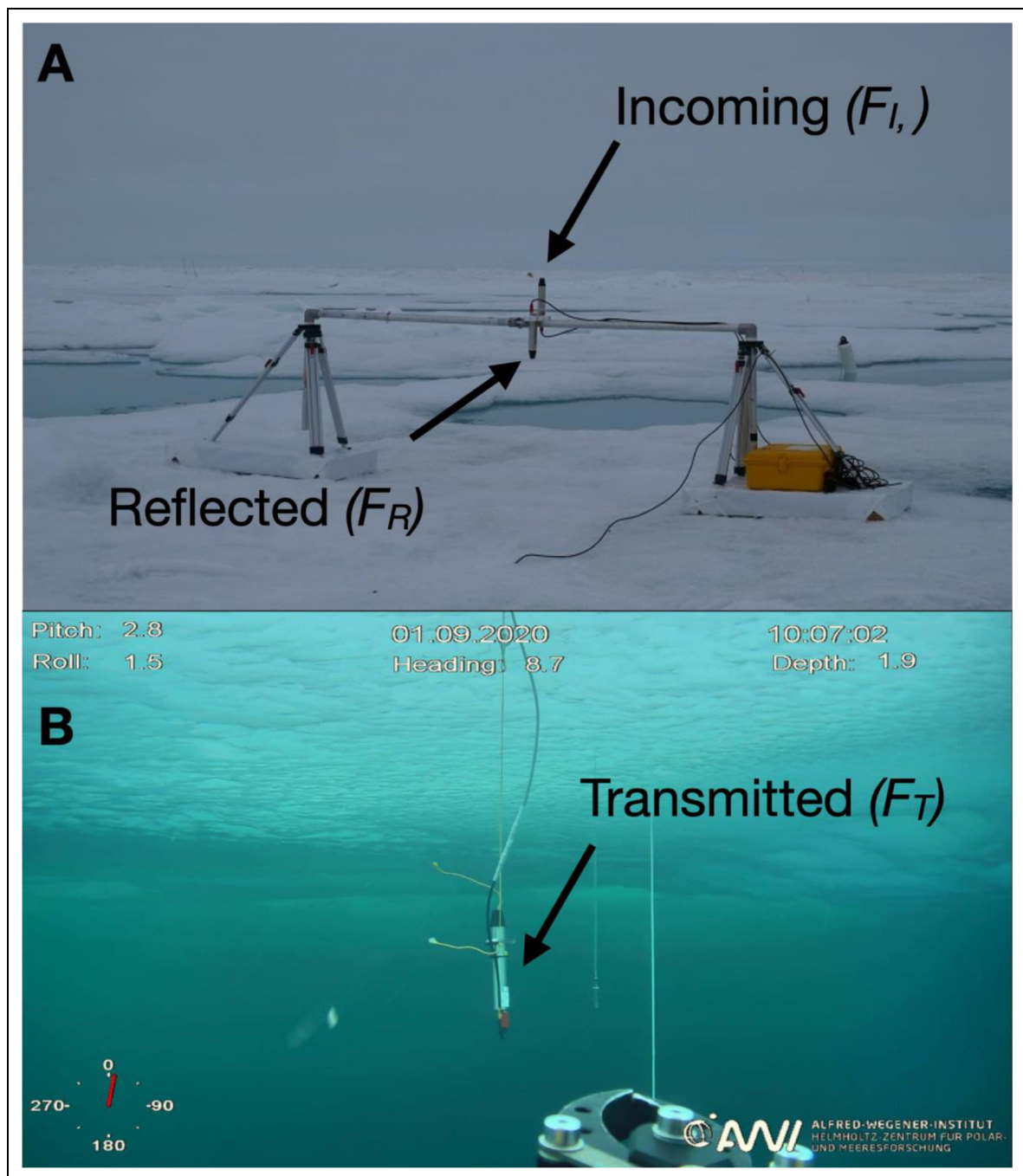


Figure 2. Photos of a radiation station set-up on and under sea ice. (A) Photograph of station 2020R15 on July 18, 2020, including the sensors for incident and reflected irradiance. (B) Photograph of station 2020R21 on September 01, 2020, showing the sensor for transmitted irradiance hanging under the ice. The photo was taken from a Remotely Operated Vehicle. Labels give attitude parameters of the vehicle. Both stations were at the Central Observatory (**Table 1**).

To investigate the long-term seasonality of apparent optical properties (i.e., albedo and transmittance), we used the optical measurement with reference to the maximum daily solar elevation angle. The radiative fluxes into and absorbed by the sea ice, E_{ice} (Equation 5) and E_a (Equation 6), were computed from each available measurement initially. Combined with the transmitted irradiance (E_d), the daily mean and accumulated radiative fluxes were used to examine the sea-ice energy budget. Sub-diurnal variations and synoptic weather events are not resolved in the presented data.

2.3. Data quality and uncertainties

During the MOSAiC expedition, the 10 autonomous spectral radiation stations were deployed at sites with different sea-ice and surface conditions. The stations were checked and maintained irregularly, but operated mostly independently. As with other autonomous instruments on drifting sea ice, some stations showed data interruption due to hardware failure (e.g., sensor or battery fault) or ice dynamics (e.g., ridging event), as recorded in **Table 1**.

The above-ice radiation sensors were leveled and mounted on a rack, which was secured to the sea ice. A

tilt due to the change of the surface or differential settling cannot be avoided during long-term measurements in a dynamic sea-ice regime. Hence, we monitored the inclination angle of the sensor over time, and excluded data with inclination angles larger than 10° . Additionally, we flagged the data as low-quality when the solar elevation angle was smaller than 5° . We also observed some noise in spectral albedo at wavelengths smaller than 400 nm, which was due to the downward-looking sensor. A detailed description of the quality of the sensor and data interpolation adopted in this study can be found in Nicolaus et al. (2010b). **Table 1** shows the operational time of each station and the resulting times with high-quality data.

Another uncertainty in this study comes from the distance between the under-ice sensor and the sea-ice bottom. The initial set-up of approximately 0.5 m was to prevent sea-ice growth from intruding on the sensor. Due to the nature of autonomous stations, the distance changed over time with ice growth/melt without sensor depth adjustment. The observed transmitted irradiance included the absorption from the top water layer, resulting in a reduction of 20% to 30% of light transmittance (Woźniak and Dera, 2007; Nicolaus et al., 2010b).

For quality control, we performed radiative transfer simulations for comparison with measured spectrally integrated E_i for all individual radiation stations during the measurement period. The modeling considered only cloudless atmospheric conditions to avoid uncertainties caused by unknown cloud microphysical and macrophysical properties, which were not available for these remote radiation stations. However, a direct comparison for cloudless days allows (i) to monitor the occurrence of clouds, (ii) to identify potential effects of sensor misalignment in cloudless conditions, and (iii) to validate the radiometric calibration. Broken cloud conditions can be identified by short-term variations of E_i , while more compact cloud situations lead to a general decrease of E_i compared to the simulations. Misalignment of the sensors can be detected by an asymmetric diurnal variation of E_i . The data were not corrected for misalignment, but instead were excluded from further analysis. In contrast to the cloud effects, uncertainties in the radiometric calibration would lead to systematic shifts in the measured E_i under cloud-free conditions compared to the simulations. However, such shifts were not observed, indicating the stability of the radiometric calibration of the upward-looking sensor.

The simulations were performed with the library for radiative transfer routines and programs (libRadtran; Mayer and Kylling, 2005; Emde et al., 2016). As a solver for the radiative transfer equation, the Discrete Ordinate Radiative Transfer solver (DISORT) (Stamnes et al., 2000) was chosen. The extraterrestrial spectrum was taken from Gueymard (2004). The meteorological input for the simulations was based on standard profiles of trace gas concentrations, air temperature, humidity, and pressure from Anderson et al. (1986). The standard sub-Arctic atmospheric profile was adapted to observations from radio soundings (Maturilli et al., 2021), which were launched about every 6 hours from *Polarstern*.

3. Results

3.1. Overview of surface properties and seasonality

Figures 3 and **4** summarize the surface conditions and seasonal evolution of optical properties for April to September, 2020, with a particular focus on the spring–summer transition from May to mid-July 2020. **Figure 3** provides the time series of the measurements of the 10 radiation stations based on daily measurements at times of the highest solar elevation angle (local solar noon). **Figure 4** shows hourly values of meteorological parameters and a summary of the surface albedo evolution until the end of July. Figure S1 shows photos of the surface conditions and radiation stations taken by autonomous cameras at sites LM and L3, and of the Central Observatory (CO) from a panorama camera (Panomax) onboard *Polarstern*. **Figures 5–7** show the seasonal evolution of spectral albedo and transmittance.

The dataset allows a particularly comprehensive analysis of the radiative fluxes of the Arctic sea ice during the spring–summer transition, a period that aligns with the maximum incoming irradiance. This study focuses on three radiation stations sited on multi-year ice (**Table 1**), which are later compared to satellite remote sensing observations. The three stations are named after their site of deployment hereinafter: LM, L3, and CO. Radiative fluxes showed an increasing spatial variability after the melt onset, mostly attributable to events (e.g., ponding and drainage; see Figure S1) which did not persist nor progress over the same time scale. This variability is well expressed in the different phases and the differences in timing and sequence of events (similar to those defined by Perovich and Elder, 2002; Nicolaus et al., 2010a) at the different stations (**Figures 3** and **4**). Overall, we distinguished three phases of the sea-ice and snow surface evolution when transitioning to the melt season:

- (a) Phase 1 (before May 26) was characterized by the mostly below-freezing point air temperature (0°C) and dry snow coverage at all three sites. Melt onset occurred on May 26, when the air temperature remained above 0°C continuously for several days and snow started to melt on the surface.
- (b) Phase 2 (May 26 to June 27) showed a strong surface spatial variability across the three sites due to events (e.g., ponding and drainage) at different times. The radiative fluxes reached their maximum during this phase.
- (c) Phase 3 (after June 28) was characterized by the formation of a weathered surface layer, known as a scattering layer from the optical perspective. The spatial variability of surface properties between the three sites decreased compared to Phase 2.

3.2. Phase 1: Dry snow surface (before May 26)

Figure 4A shows that the air temperature reached the melting point (0°C) for two short intervals in April but regularly and for longer times after May 12. The surfaces of the three sites were covered by dry snow in April, for example, Figure S1A and B.

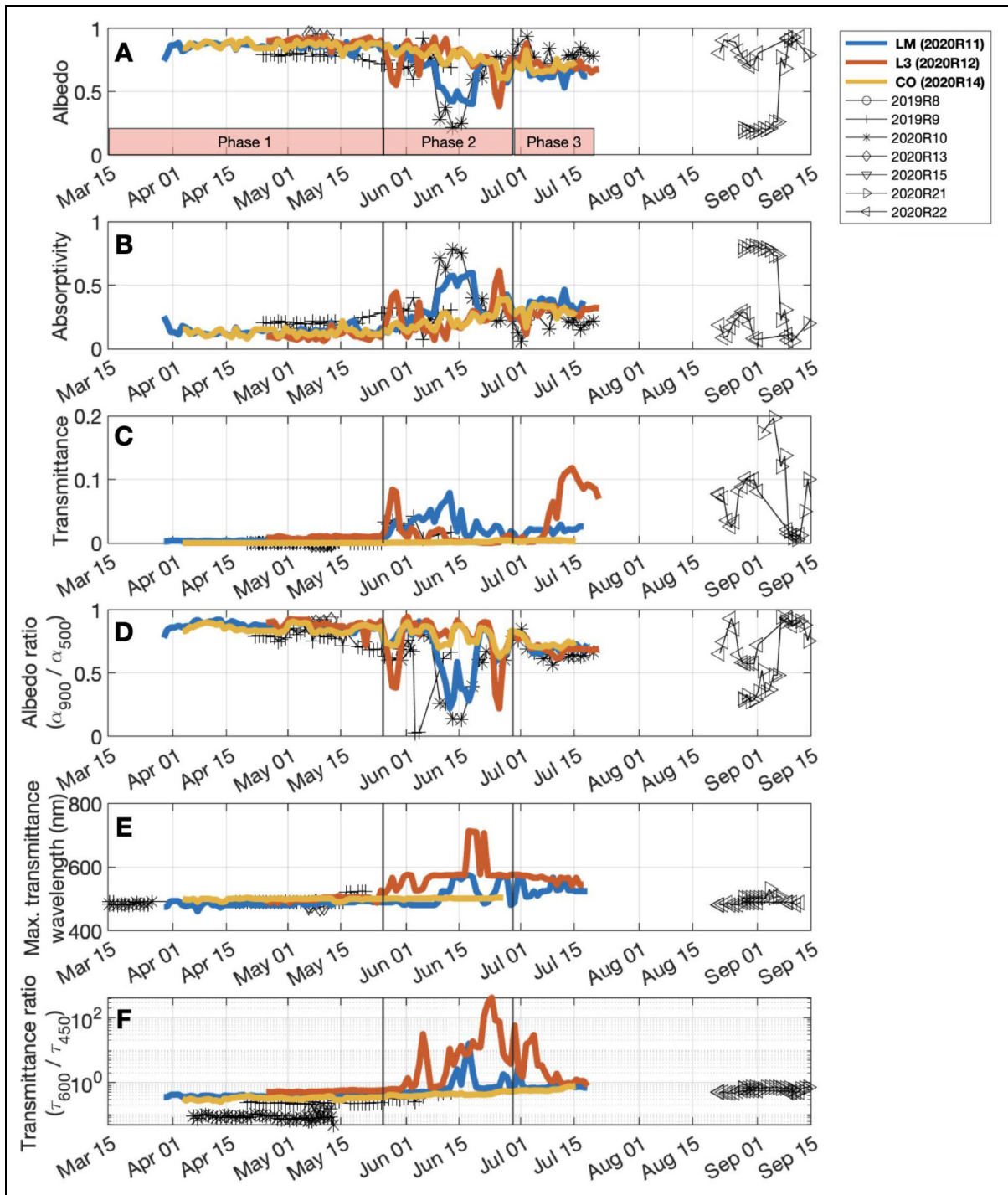


Figure 3. Seasonal progression of optical properties measured by radiation stations during the sunlit season in 2020. Lines show wavelength-integrated (350–920 nm) values of (A) surface albedo, (B) surface and ocean absorptivity, (C) transmittance, (D) albedo ratio of 900 to 500 nm ($\alpha_{900}/\alpha_{500}$), (E) wavelength of the maximum transmittance of each spectrum, and (F) transmittance ratio at 600 to 450 nm (τ_{600}/τ_{450}). The three radiation stations with continuous records are highlighted in color: 2020R11 at the LM site (blue), 2020R12 at the L3 site (red), and 2020R14 at the CO site (orange). The two black vertical lines indicate the melt onset (May 26) and the stage of advanced melt and formation of surface weathered layer (June 28).

From April 1 to May 25, the mean broadband albedo at all three sites was as high as 0.89 with a standard deviation of 0.03. Compared to later phases, the three sites had the most similar optical properties and most homogeneous surface conditions, although sea-ice thickness ranged from 1.59 m to over 3 m. The spectral albedo was

higher than 0.80 over the entire wavelength range from 350 nm to 920 nm (e.g., **Figure 6** shows the spectral albedo on May 1 at sites LM and L3). The mean albedo ratio was 0.87 (± 0.03) (**Figure 3D**).

The broadband transmittance was lower than 0.05 for all sites. The shape of spectral transmittance,

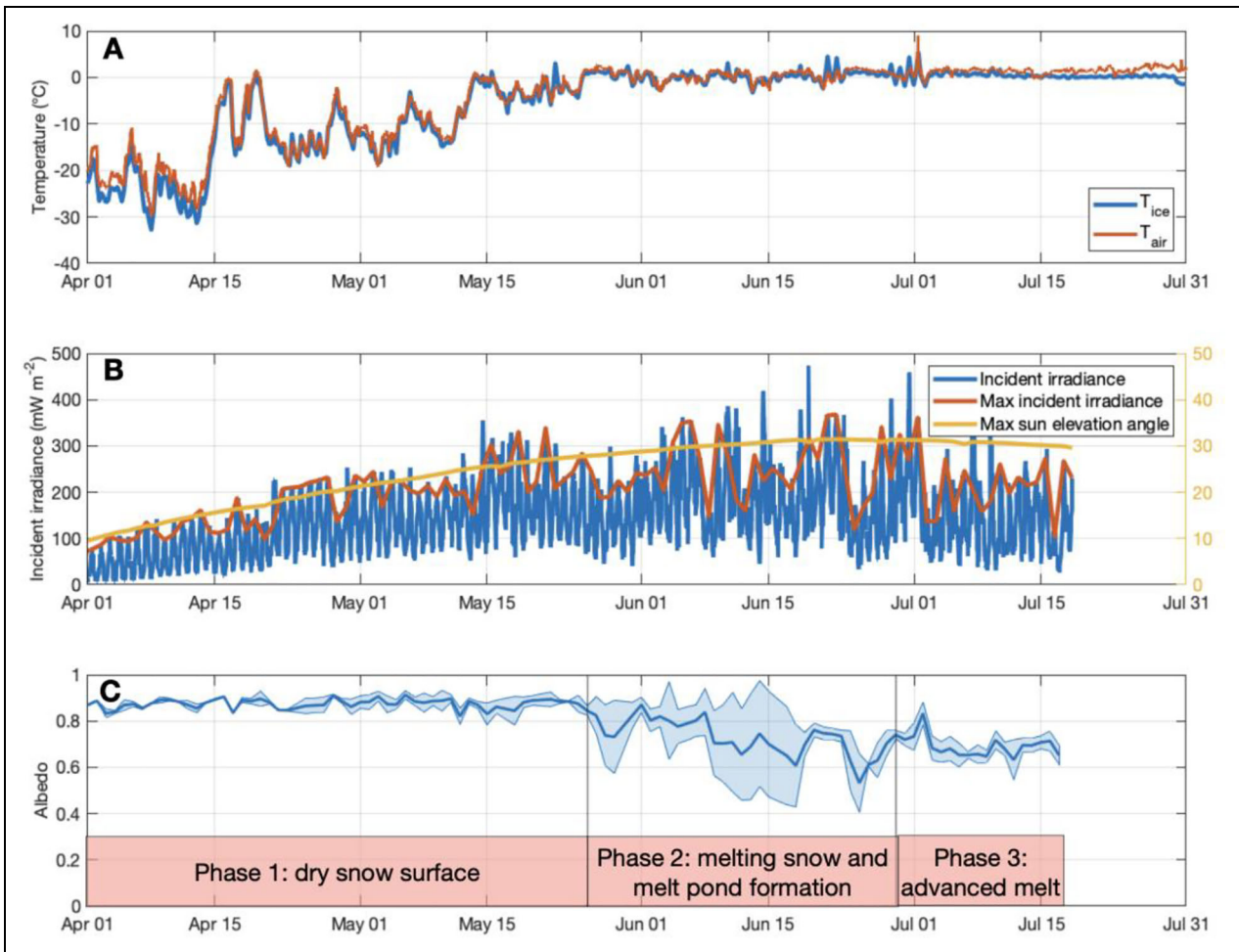


Figure 4. Evolution of surface properties from April to July 2020. (A) Air temperature from ice-mass-balance buoy 2020M29 and sea ice temperature snow buoy 2019S94. (B) Incident solar irradiance from radiation station 2020R11. (C) Mean and standard deviation of total albedo from the three radiation stations at sites LM, L3, and CO: 2020R11, 2020R12, and 2020R14, respectively. The red-shaded areas mark the three phases.

particularly at wavelengths centered around 490 nm, suggested no influence of biological activity (Figure S1E and F; Figure 7).

3.3. Phase 2: Melting snow and melt pond formation (May 26 to June 27)

Melt onset was detected on May 26 and snow started to melt on the surface (e.g., Figure S1D), as defined in Perovich and Elder (2002). During Phase 2, the most prominent feature was the high spatial variability in the optical properties between the different sites. This variability is well expressed in differences in timing and the sequence of ponding events. Three melt ponds (MP) were recorded: MP1 at site LM, MP2 at site L3, and MP3 again at site LM.

Overall, the three sites showed a decrease in albedo at different scales, with the maximum decrease at each site spanning from 27% due to melting snow to 51% due to ponding events (Figure 3A). Site CO showed a linearly decreasing broadband albedo and no ponding event. There were three individual ponds (MP1, MP2, MP3) that formed within the fields of view of the E_u sensors at sites LM and L3 (e.g., Figure S1E, H, and N). Events such as pond formation and later pond drainage increased the spatial variability of

surface conditions during Phase 2. Also, the albedo at wavelength above 500 nm (the albedo ratio) showed a decrease due to the increasing liquid water on the surface (Figure 3D). The transmittance at sites LM and L3 showed an increase and change in the spectral shape.

MP1: First melt pond 1 at site L3:

At site L3, MP1 formed immediately after the melt onset (Figure S1E). Over MP1, broadband albedo decreased to 0.58 from 0.84 (−31%). The shape of the spectral albedo changed drastically from a rather linear- to a dome-shape, and the spectral albedo at a wavelength larger than 500 nm decreased below 0.67 (May 29; Figure 6). This decrease resulted in the albedo ratio decreasing to 0.39. The broadband transmittance peaked at 0.08, and the wavelength of the maximum transmittance increased to 526 nm, compared to 496 nm during Phase 1 (Figure 3E).

On June 1, a thin new snow layer was observed (Figure S1F and G), and site L3 showed an increase in broadband albedo to 0.87 and a decrease in broadband transmittance to 0.010. The shape of spectral transmittance showed a strong change (Figure 3E and F). On June 5, the maximum wavelength of transmittance increased to 576 nm,

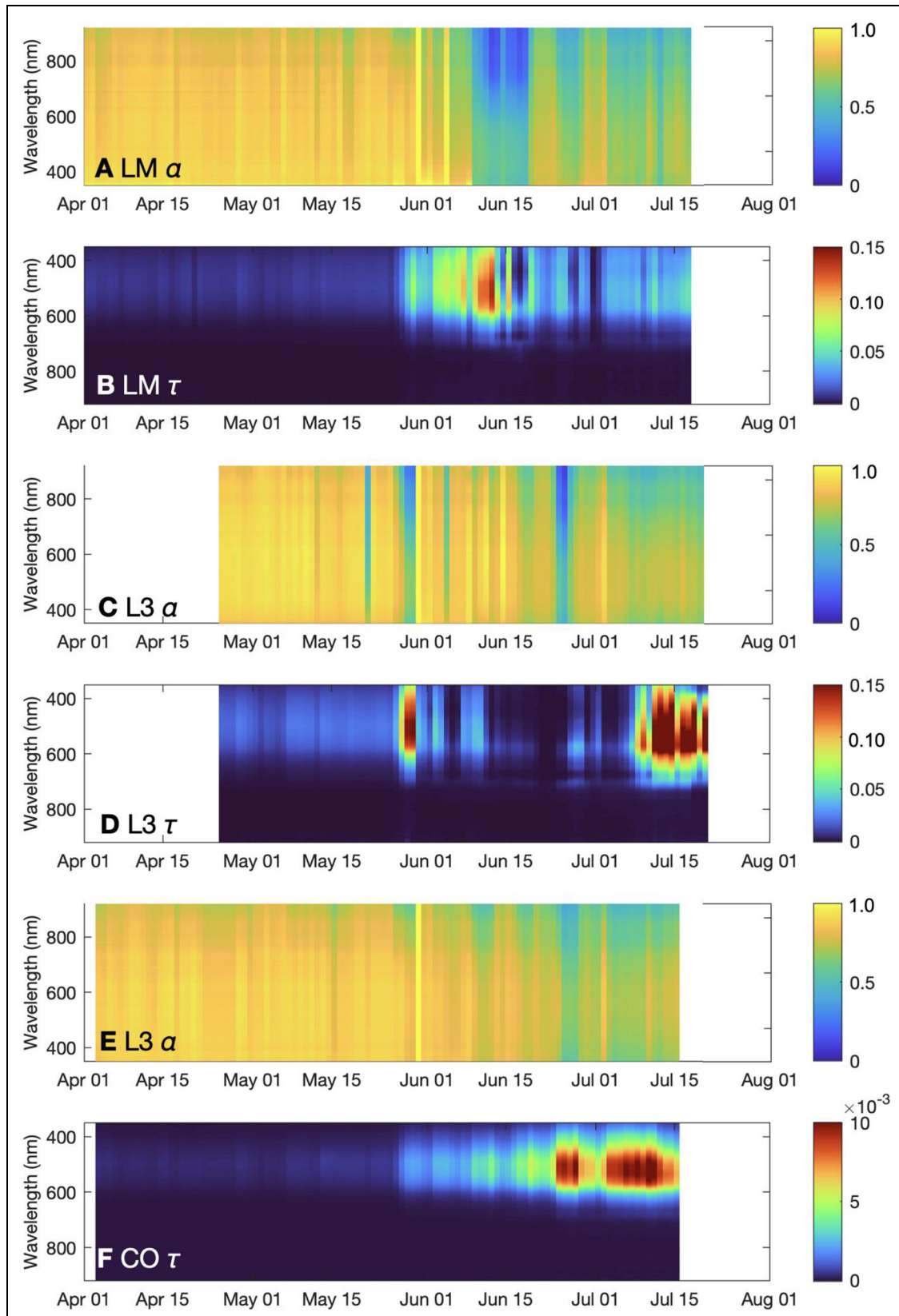


Figure 5. Spectral albedo and transmittance of sea ice from three stations during spring–summer 2020. One spectrum is shown per day, from the measurement at the time of highest solar elevation. Results for each site are shown in two panels, one for spectral albedo (α) and one for spectral transmittance (τ): panels A and B for site LM; C and D for site L3; and E and F for site CO. Note the different scale of transmittance for panel F.

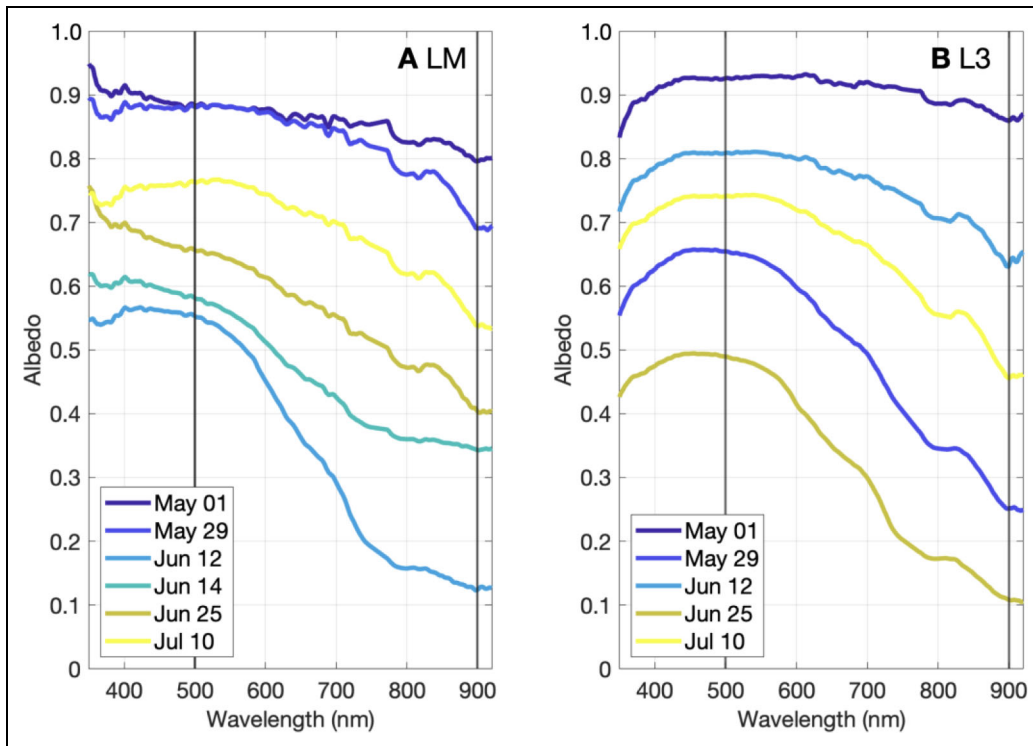


Figure 6. Albedo spectra at two sites for selected dates in spring-summer 2020. Albedo spectra from radiation stations at (A) site LM and (B) site L3. The solid vertical lines highlight the wavelengths of 500 nm and 900 nm because of their relevance for the $\alpha_{900}/\alpha_{500}$ ratio (Figure 4D).

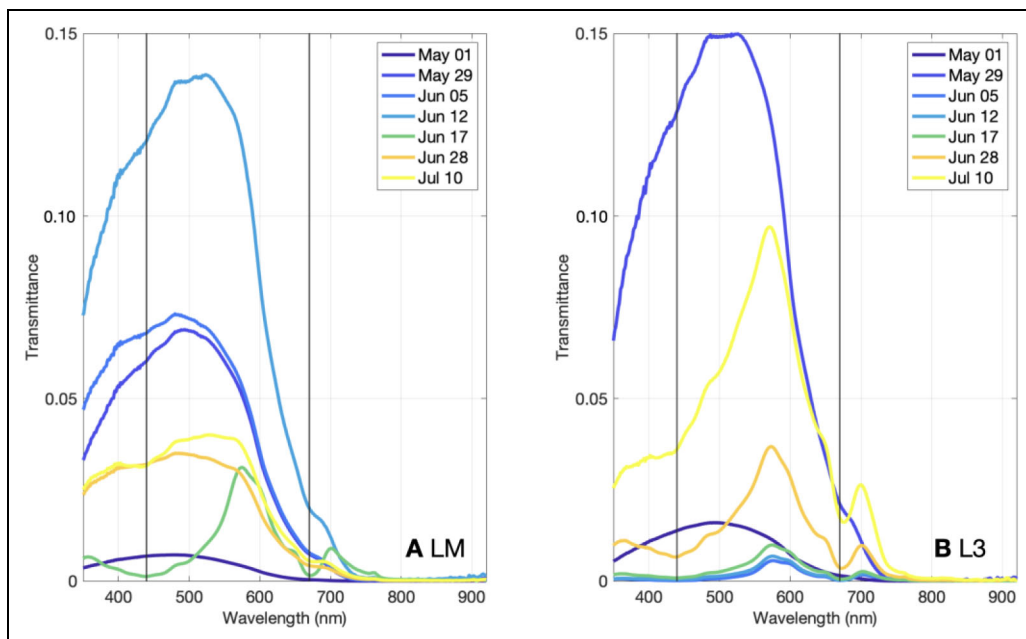


Figure 7. Transmittance spectra at two sites for selected dates in spring-summer 2020. Transmittance spectra from radiation stations at (A) site LM and (B) site L3.

and the transmittance ratio peaked at 31.47, which aligns with the high absorption coefficient of under-ice biomass at wavelength centered around 440 nm (e.g., Perovich et al., 1993; Lund-Hansen et al., 2015). Compared to Phase 1 (May 1), the spectral transmittance on June 5 showed

two strong decreases, centered around 440 nm and 670 nm (Figure 7).

MP2: Melt pond at site LM:

From June 5 onward, mean broadband albedo generally decreased again with an increasing spatial variability

(**Figure 3A**). The melt pond event at site LM (MP2; **Figure S1H**) led to a decrease of its broadband albedo to 0.44 from 0.73 (−39%). A strong decrease in albedo was found at wavelengths larger than 550 nm, resulting in the minimum albedo ratio of 0.22 (**Figure 3D**). On June 14, a new snow layer increased the broadband albedo at site LM for a day, and the albedo ratio increased temporally to 0.59.

The broadband transmittance at site LM increased to 0.079 from less than 0.01 in 2 weeks. The shape of spectral transmittance showed a stronger variability (**Figure 3C, E, and F**) after June 14, when the broadband transmittance started to decline from its maximum. For instance, on June 14, the transmittance ratio increased rapidly with the decreasing broadband transmittance and peaked at 16.0 (**Figures 3F and 7A**).

On June 17, site L3 showed a similar shape of spectral transmittance. The change in the shape of spectral transmittance persisted toward June 23, when the maximum wavelength of transmittance peaked at 710 nm, and the transmittance ratio peaked at 421 (**Figure 3E and F**).

MP3: Second melt pond at site L3:

At site L3, a ponding event was again observed (e.g., **Figure S1N**), resulting in a minimum albedo of 0.38 on June 25, after a rapid decrease from 0.70 on June 23 (45%). The albedo ratio reached the minimum of 0.22 (e.g., **Figure 6A**).

Broadband transmittance remained lower than 0.012 during the formation of MP3. Compared to MP1 (also at site L3), even with the minimum albedo and more light to the ponded surface, the transmittance during MP3 was significantly lower than 0.080. Site L3 showed an absorptivity as high as 0.61 during MP3, compared to 0.34 during MP1. The spectral transmittance showed a similar spectral shape compared to June 23, with the maximum wavelength at 707 nm and a transmittance ratio of 77.0 (**Figure 3E and F**).

3.4. Phase 3: Advanced melt (after June 28)

From June 28 onward, the three sites showed surface drainage and a weathered ice layer, resulting in a broadband albedo with an increasing temporal consistency and a more linear decline with less spatial variability (**Figure 3C**). From June 28 to July 18, the mean broadband albedo from all three sites was 0.69 (± 0.05 ; **Figure 3A**). The spectral albedo showed a similar shape during this phase (e.g., **Figure 6**). The mean albedo ratio (**Figure 3D**) increased to 0.81 (± 0.02) on June 28, and then decreased to 0.73 (± 0.02) on July 15.

The broadband transmittance showed larger spatial variability, mainly attributed to the formation of a lead in the proximity of site L3 (**Figures 3C and S1T**). At site L3, the spectral transmittance also showed a stronger change than at the other two sites (**Figure 7**); for example, two distinctive decreases centered around 440 nm and 670 nm were shown on June 28. On June 30 and July 5, the transmittance ratio at site L3 showed two peaks at 57.8 and 29.5. At site LM, the shape of spectral transmittance did not change as strongly, with a transmittance

ratio of 0.6 that remained so until July 15 (**Figure 3E and F**).

3.5. Summary of progression

Summarizing the results of three individual time series, we find a general progression from spring to summer conditions with the broadband albedo ranging from 0.38 to 0.97 and transmittance from less than 0.010 to 0.120 across three sites. After the melt onset, we find an increasing surface variability from the three sites, particularly at sites LM and L3 (compared to site CO, which showed only a more linear evolution), driven by ponding events. Under the same atmospheric conditions, the timing and effects of events vary by site. Individual events, such as pond formation and drainage, and lead formation (e.g., **Figure S1T**) have effects, which lead to the short-term decrease of albedo and an increase in absorptivity and transmittance. At the same site, the energy partitioning between transmittance and absorptivity during different ponding events was different. For instance, the transmittance at site L3 only increased by a small amount with the formation of MP3 as the under-ice sensor was least affected. We also examined the temporal evolution of the spectral albedo and transmittance, and distinguished the radiative fluxes into and through the snow and sea-ice surface when the Arctic was transitioning from spring to summer.

3.6. Seasonality of the surface evolution and surface fluxes

Figure 8 shows the daily averaged broadband irradiances (incident, penetrating into the sea ice layer, Equation 5; absorbed by the ice layer, Equation 6; and transmitted through the ice layer) during the transition from spring to summer conditions. **Figure 9** shows the daily mean of absorbed and transmitted irradiance of the three phases and individual events.

Phase 1 was characterized by the high albedo and increasing solar irradiance (e.g., **Figure 4A and B**). We computed the accumulated energy being deposited into the snow and sea ice surface (surface influx) during a 31-day period from April 25 to May 25, when all three sites were recording data. With the mean albedo of 0.89, the daily mean energy entering the snow and sea ice was smaller than 2 MJ m^{−2} for all three sites. Throughout the entire Phase 1, which showed rather homogeneous surface conditions compared to later phases, the accumulated energy budget differed between the sites. For instance, during the entire Phase 1, site LM showed 35.6% (15 MJ m^{−2}) more energy deposited into the surface than at site L3.

After melt onset, the highest incident irradiance and surface influxes were observed (Phase 2). The three sites showed a mean surface influx of 3.7 (± 1.1) MJ m^{−2} day^{−1}, almost twice as much as during Phase 1. Site LM showed the highest daily surface influx (5 MJ m^{−2}), mostly contributed by the 15-day duration of MP2. MP2 increased the daily surface influx at site LM by 35% compared to the other two sites during the entire Phase 2. Sites L3 and CO showed a daily surface influx of 3.2 MJ m^{−2} and 3.1 MJ m^{−2}, respectively.

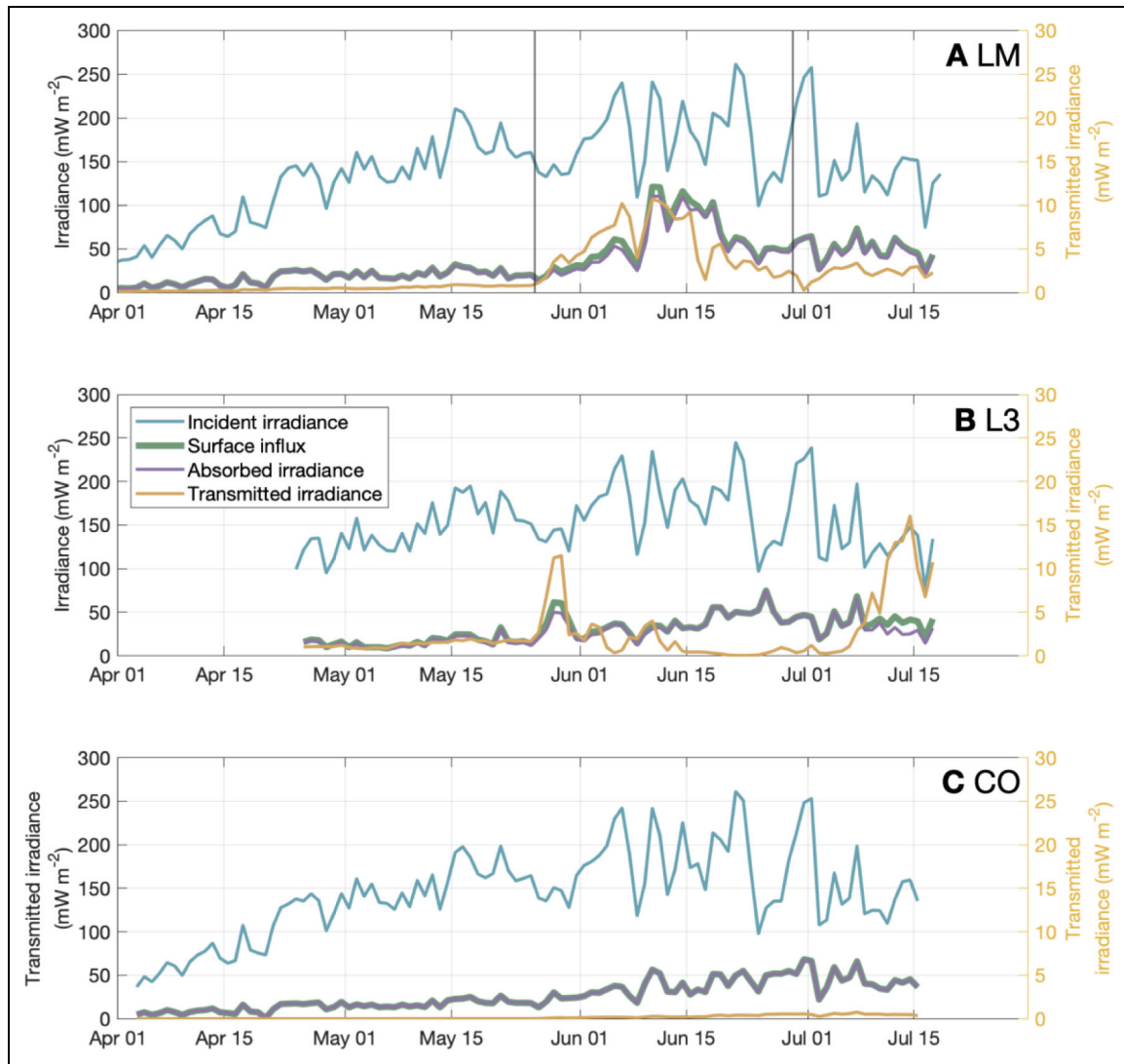


Figure 8. Seasonal evolution of the radiative fluxes of sea ice at three sites during spring–summer 2020. Daily mean of incident irradiance, flux into the surface, absorptance by sea ice plus the uppermost ocean, and transmitted irradiance into the ocean at (A) site LM, (B) site L3, and (C) site CO. The transmitted irradiance is plotted on the right y-axis. In panel A, the two black vertical lines indicate the melt onset (May 26) and the stage of advanced melt and formation of surface weathered layer (June 28).

During the ponding event of MP2 (14 days), site LM showed a daily surface influx of 7.2 MJ m^{-2} (Figure 9B), about twice that of site L3 during MP1 and MP3 (3.4 MJ m^{-2} and 3.7 MJ m^{-2} , respectively). The total surface influx at site LM during the MP2 event was 100.8 MJ m^{-2} ; that is, 99% of the CO during the entire Phase 2 (33 days). Hence, a temporally limited ponding event can impact the summer radiative energy budget as much as the seasonal evolution over a month.

As the surface melting progressed and the albedo decreased at all three sites, the impact of melt ponds (e.g., MP3) on increasing the surface influx became less. For instance, during the formation of MP3, site L3 showed a surface influx of $3.7 \text{ MJ m}^{-2} \text{ day}^{-1}$, while the other two unponded sites both showed a mean surface influx of $3.2 \text{ MJ m}^{-2} \text{ day}^{-1}$.

Phase 3 is characterized by the weathered surface layer at the three sites after surface drainage. The mean daily

surface influx was $3.7 (\pm 0.2) \text{ MJ m}^{-2}$. The surface spatial variability between the three sites decreased during this phase. Also, a lead formed within 5 m of the L3 station, which increased the irradiance underneath the ice.

4. Discussion

4.1. Seasonality of energy deposition and melt rates

After melt onset, the surface influx increased at all sites, but not linearly or regularly. The strong contrast in the seasonal evolution shown by the three stations resulted from the very patchy surface evolution at the individual sites. During the melt season, absorptivity and transmittance varied between individual events (Sections 3.3 and 3.4). The energy partitioning between in-ice absorptivity and transmission into the ocean varied significantly, impacting the primary internal ice melt rate.

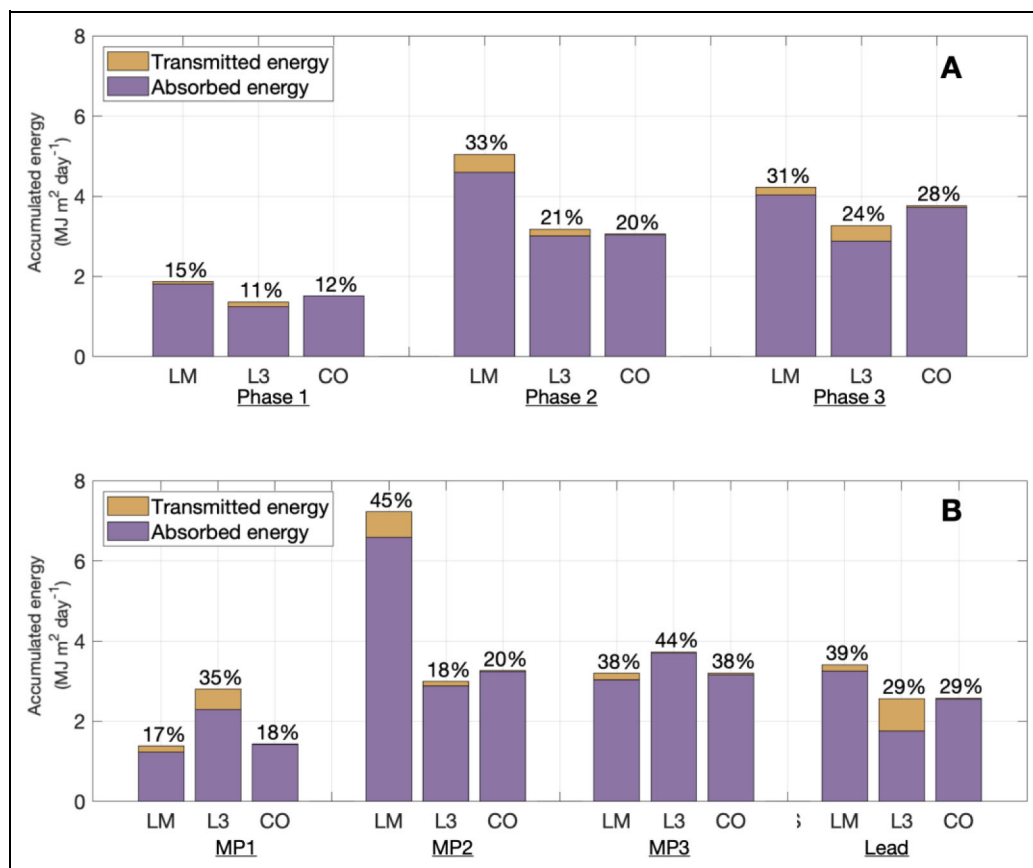


Figure 9. Daily mean of absorbed and transmitted irradiance at three sites. (A) Integrated values during Phase 1 (April 25 to May 26), Phase 2 (May 26 to June 29), and Phase 3 (June 30 to July 15). (B) Integrated over individual events: MP1, first ponding event at site L3 (May 26 to May 29); MP2, ponding event at site LM (June 4 to June 19); MP3, second ponding event at site L3 (June 25 to June 29); and lead formation near site L3 (July 10 to July 15). Above each bar is shown the percentage of energy deposition (total of absorbed and transmitted) to mean solar incoming energy during each phase and event.

In Phase 2 after melt onset, the sea ice received the largest energy deposition, when the mean absorbed irradiance by the ice and the top ocean layer was $3.7 (\pm 1.1)$ $\text{MJ m}^{-2} \text{ day}^{-1}$ (Figure 9). In a span of 33 days, the total absorbed solar energy was $120 (\pm 30)$ MJ m^{-2} . The accumulated absorbed irradiance during Phase 2 has the potential to melt a column of sea ice by as much as $45.5 (\pm 11.7)$ cm. The mean transmittance during this phase was 0.015, integrating to a total of 7.4 MJ m^{-2} , a potential bottom melt of 2.8 cm.

During the entire Phase 2, site L3 showed a total absorbed energy of 102.0 MJ m^{-2} and total transmitted energy of 5.9 MJ m^{-2} . MP1, showing a duration of 5 days from May 26 to June 1, resulted in a total absorbed energy of 12.8 MJ m^{-2} and transmitted energy of 2.8 MJ m^{-2} . Having a similar duration in late June (23 to 28), MP3 resulted in a total absorbed irradiance at site L3 of 27.7 MJ m^{-2} and total transmitted energy of only 0.2 MJ m^{-2} . Comparing to MP1, MP3 showed a higher amount of radiative energy deposition due to the changing incident irradiance. Also, the majority of the radiative energy was absorbed by the sea-ice layer during MP3 event, rather than being transmitted into the ocean. Computing the entire Phase 2 (34 days), site L3 had the

potential for internal and bottom ice melt of 38.7 cm and 2.0 cm, respectively.

During the entire Phase 2, site LM showed the largest absorbed energy of 156.0 MJ m^{-2} due to the formation of MP2, enough to melt 59.0 cm of ice. The transmitted energy was 15.5 MJ m^{-2} , equivalent to 5.9 cm ice melt from the bottom. The ponding event (MP2) accounted for a significant portion of the total absorbed and transmitted energy of 97.0 MJ m^{-2} and 9.7 MJ m^{-2} , which had the potential to melt 36.7 cm and 3.7 cm ice internally and from the bottom, respectively.

During Phase 3, the three sites accumulated a mean absorbed energy of 60.3 MJ m^{-2} , equivalent to a 22.8 cm internal ice melt. The transmitted energy showed a higher variability due to the lead formation near site L3 (e.g., Figures S1 and 9B). Within 16 days, site L3 accumulated a transmitted energy of 6.6 MJ m^{-2} , enough to melt 2.5 cm ice.

Overall, site LM showed by far the strongest absorbed irradiance, and thus ice melt. Although sites L3 and CO showed a similar amount of energy deposition into the sea-ice surface, the bottom melt rate of site L3 was higher than site CO due to the higher transmitted irradiance. Having no ponding event and small transmitted

irradiance, site CO experienced a bottom melt rate an order of magnitude smaller, as its transmittance remained a minimum.

4.2. Effects of melt ponds

In this study, we examined the energy partitioning of three sites with different snow, ice, and surface conditions during the spring–summer transition. Commonly, melt onset was on May 26, initiating a phase of strong spatial variability with little temporal consistency. As a result, the energy partitioning showed a strong variability, driven by melt pond formation and drainage at different sites and with different timing.

The locations of melt ponds depend on surface topography. Melt ponds from the previous year have the potential to pre-condition the location and size of new melt ponds (Webster et al., 2022; Thielke et al., 2023). However, at the time of installation of the stations, when or even if ponds might form in the field of view of the E_{μ} sensor, which has a footprint of only 1 m², was not foreseeable. As a result, the described optical properties and melt pond evolution are not necessarily representative of a region larger than the field of view of the RAMSES sensors. Having internally consistent results for the three long-term stations, we find the same characteristics during the three phases. This finding is also supported by other stations, for example, 2020R10 (Figure 3A), which also showed a ponding event and minimum albedo observation in mid-June, similar to MP2 at site LM.

The three stations in this study were on second-year ice, and the differences in seasonal evolution were due to the heterogeneous ponding events. There was an increasing surface spatial variability on the floe scale, starting in late May. The melt pond fraction increased to over 20% in late June (Webster et al., 2022), followed by a temporary decrease due to drainage. Based on measurements from the three radiation stations, we defined Phase 3 with a start date in late June. However, the surface drainage was not homogeneous for the entire ice floe. In July, the melt pond fraction increased and reached the maximum (Webster et al., 2022).

4.3. Representativeness of radiation station measurements

In this study, we focused on three stations that succeeded in capturing the spring–summer transition in 2020 as planned. They were on multi-year (second-year) ice. The evolution of sites LM and L3 was strongly impacted by abrupt changes in melt pond conditions, and thus strongly event-driven. By comparison, site CO showed a rather linear seasonal progression, but site CO also had the thickest ice.

These results are representative of multi-year ice with similar conditions, but not of the entire ice floe. We were not able to obtain measurements on thin ice, which melted completely in July. Considering the peak solar irradiance, there would be a large amount of energy deposited into the ice and the ocean via the thin ice when transitioning into the summer. Taking into account the

expanding and deepening of melt ponds from mid-June (Webster et al., 2022) and later pond drainage (e.g., Light et al., 2022) over a larger floe-size scale, the surface heterogeneity can impact the energy budget of sea ice during the melt season and can alter the location of sea-ice melt.

Furthermore, the MOSAiC ice floe showed a thinner ice thickness compared to the surrounding and historical records along the same trajectory (Kruppen et al., 2020; Kruppen et al., 2021). This relative thinness indicated an earlier melt onset and earlier melt pond formation (Kruppen et al., 2021). Figure 10A shows the melt onset date of the MOSAiC stations along with satellite data. Compared to the satellite record, the MOSAiC melt onset was earlier (May 26), comparing to other points with the same latitude (6th percentile).

Also, a lead was formed within 5 m of site L3 in July, which increased the observed transmitted irradiance as the light was scattered horizontally. The surface albedo at site L3 was unaffected. Such an event could not represent the pure physical evolution of radiative fluxes of sea ice, but only a single unrepresentative case.

This study provides insights into the spectral albedo and transmittance of different sea-ice types, which is important to understand the solar partitioning over an aggregate scale. We recommend future work to expand this result to a larger area (e.g., aerial images), in order to improve sea-ice classification, and to extend the observation period. This expansion will require a wider range of ice conditions, in particular including thin and melting ice.

4.4. Comparison to earlier studies

Figure 10 compares the seasonality of melt onset date and albedo from the MOSAiC observations to the Tara (Nicolaus et al., 2010a) and SHEBA (Perovich and Elder, 2002) expeditions, as well as to satellite remote sensing data from 1998 to 2020. Having multiple stations, we are able to investigate the seasonality and, more importantly, the scale of spatial variability of radiative partitioning during this period.

The best comparable dataset is from the Tara expedition (Nicolaus et al., 2010a), which is based on a radiation station with the same set-up and sensors as in this study. Also, the Tara station showed a similar surface type to the LM station. The Tara station was deployed on 2 m thick ice and snow and drifted from 88.2°N on April 29, 2007, to 87.8°N on August 1, 2007. Nicolaus et al. (2010a) derived a melt onset on June 10, 15 days later than during MOSAiC. After the melt onset, the Tara albedo first showed an almost linear decrease until reaching its minimum on July 1, with the surface drainage occurring on July 3. The mean surface flux transitioned from 45.5 W m⁻² to 54.5 W m⁻² during this period (Nicolaus et al., 2010a). During the corresponding phase (Phase 2) of the MOSAiC observations, the mean surface flux ranged from 35.4 W m⁻² (site CO) to 58.1 W m⁻² (site LM). The MOSAiC sites, LM and L3 in particular, showed an earlier and more episodic evolution than the Tara station due to various melt pond events. The maximum transmittance

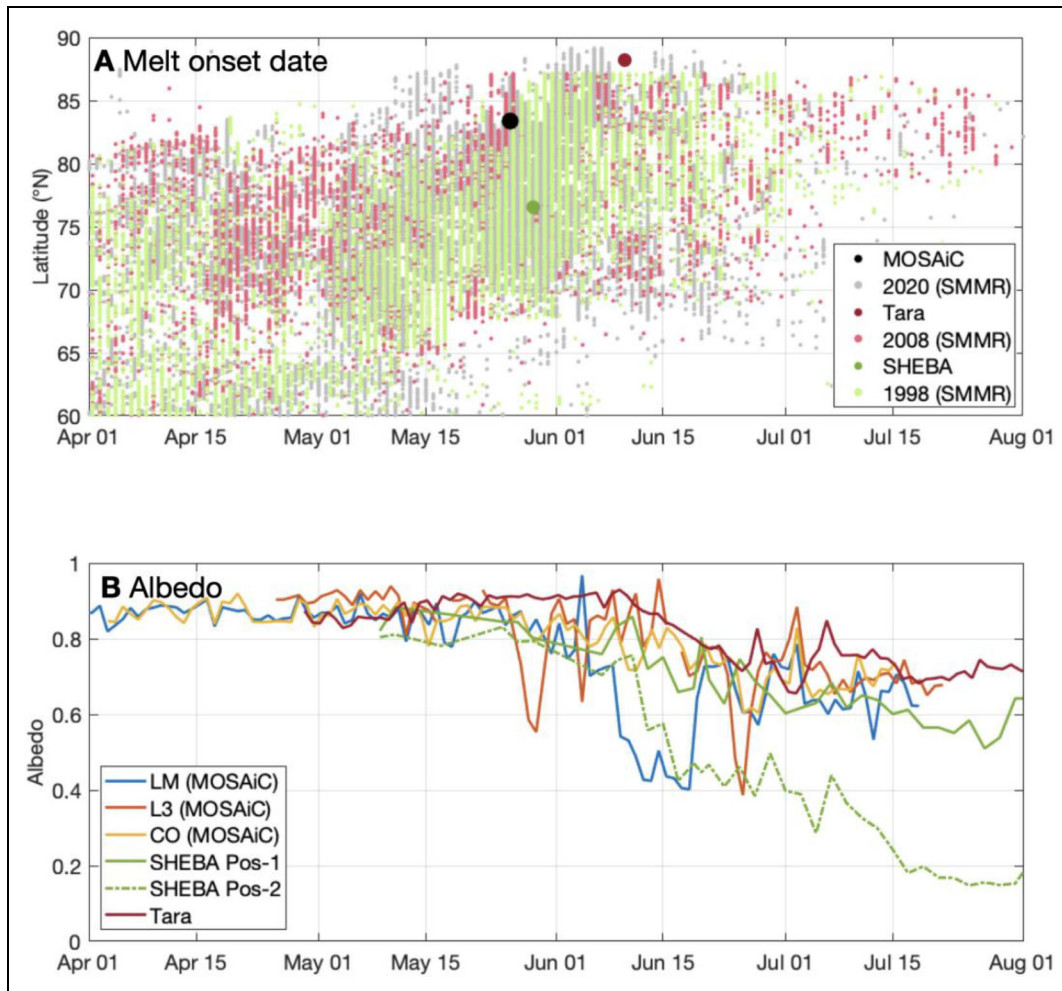


Figure 10. Seasonal evolution of melt onset date and surface albedo during spring–summer 2020. (A) Melt onset from the MOSAiC, Tara (Nicolaus et al., 2010a) and SHEBA (Perovich and Elder, 2002) expeditions, with melt onset dates from each dataset shown in bigger black (MOSAIC), red (Tara) and green (SHEBA) dots. The lighter and smaller dots illustrate the melt onset dates acquired from the Scanning Multichannel Microwave Radiometer (SMMR; Anderson et al., 2019) of each respective year. (B) Albedo measurements from the MOSAiC, Tara (Nicolaus et al., 2010a) and SHEBA (Perovich and Elder, 2002) expeditions when transitioning into the melt season. The SHEBA albedo is extracted as 2 fixed positions (Pos-1 and -2) from the albedo line observation.

showed a linear increase at the Tara station, reaching its maximum (0.66) on July 1. Compared to the Tara station, sites LM and L3 showed a higher maximum transmittance at an earlier date, due to melt pond events in late May and mid-June. Overall, sites LM and L3 showed a similar seasonality to the Tara station, while site CO showed lower solar fluxes as it was on thicker ice. Integrating over a common period from May 26 to June 28, same as the Phase 2 of the MOSAiC stations, the Tara station showed an accumulated absorbed irradiance of 98 MJ m^{-2} , lower than the MOSAiC stations (which showed a mean of 120 MJ m^{-2}). The absorbed irradiance at the Tara station has the potential to melt 37.4 cm of sea ice. The lower radiative energy at the Tara station was due to the later melt onset date.

The SHEBA experiment drifted in the Beaufort and Chukchi seas, from 76°N in April 1998 to 78°N at the end of July 1998 (Perovich et al., 1998). It represents sea-ice conditions at lower latitudes 20 years earlier. The SHEBA melt onset was 3 days later, on May 29 (Perovich

and Elder, 2002). We extracted 2 points from its albedo line to show the evolution of a bare ice surface and melt pond. After the melt onset, the albedo showed a steady decrease until June 13, when the albedo started to decrease more strongly at different scales between the three sites. With the melt pond darkening, a minimum albedo of 0.18 was reached by the end of July. Beyond that, during the entire extent of the SHEBA observations, the minimum albedo of 0.1 was reached in mid-August (Perovich and Elder, 2002). On the other hand, the MOSAiC dataset (e.g., at site L3) showed a stronger evolution directly after the melt onset date, with the formation of MP1 and albedo reaching 0.58, about 15 days earlier than the SHEBA dataset.

The MOSAiC data set stands out for having multiple stations that monitor radiative fluxes above and under sea ice of different ice conditions, but with the same atmospheric forcing. As a result, our measurements describe a broader range of radiative fluxes of sea ice than a single

time series, highlighting variability. This variability is particularly important when the ice is transitioning into the melt season, with peak solar irradiance, and more energy deposition into the sea ice with a higher spatial variability.

5. Conclusions

In this study, we have presented the seasonal evolution of radiation fluxes during the spring–summer transition at multiple sites during the MOSAiC expedition in 2019–2020. Observations at these sites provided spectral radiative fluxes on and through different sea-ice, snow, and surface conditions during most of the sunlit period. We focused on the seasonal progression during the spring–summer transition by investigating the three radiation stations with continuous records from April 1 to July 18, 2020.

From these results, we identified three phases:

- (i) Phase 1: Dry snow surface before melt onset on May 26. The three sites were characterized by high albedo and small radiative net influx with a small spatial variability.
- (ii) Phase 2: Melting snow and melt pond formation. After melt onset, the air temperature was positive for several days and melting snow increased the liquid water content at the surface. Phase 2 showed the strongest spatial variability due to ponding events (MP1, MP2, and MP3), which differed from the previously defined seasonality (e.g., Perovich and Elder, 2002; Nicolaus et al., 2010a) that separated “melting snow” and “melt pond formation”. Phase 2 showed a mixture of surface evolution of reoccurring ponding events (e.g., site L3) and melting snow over sea ice (e.g., site CO). The evolution of net surface influx during Phase 2 was mostly event-driven and neither linear nor continuous. Ponding events might directly increase absorptivity but not light transmittance.
- (iii) Phase 3: After melt pond drainage on June 29. The three sites showed a steadily decreasing albedo and less variability in the absorptance of the radiative fluxes. However, the transmitted irradiance at site L3 peaked due to the lead that formed in its proximity, which enhanced the bottom melt rate by an order of magnitude compared to Phase 2.

Having multiple observation stations, we were able to investigate the solar partitioning of different ice surface conditions. We found that the impact of ponding events on radiative energy deposition into the sea ice and ocean is equally important to the seasonality of surface evolution. Melt pond formation can reduce the local surface albedo by 31% to 45%, leading to more radiative energy being deposited. For instance, a single ponding event (e.g., MP2) accounted for a surface influx as high as the unponded site CO during the entire Phase 2. Throughout the entire Phase 2, site LM showed 35% higher energy deposition than adjacent bare ice, due to a single ponding event. The strong spatial variability between different ice

types and surface conditions can impact the large-scale energy budget.

The time series shows strong spatial and temporal variations. On the spatial scales of kilometers, as used for general circulation models (GCM) or satellites, melt onset is usually defined as one specific date for the area. Our radiation stations show that the earliest detected melt is not a good predictor for the large-scale melt onset and that locations with the longest melting season (in our case L3) are not necessarily experiencing the strongest accumulated net surface flux and ice melt over the season (which in our case was site LM). Therefore, the high spatial and temporal variability we found needs to be taken into account when interpreting larger scale Arctic-wide datasets.

Data accessibility statement

The MOSAiC radiation stations data are available on PANGAEA (Tao et al., 2023, <https://doi.pangaea.de/10.1594/PANGAEA.949556>). The ice mass balance station 2020M29 can be accessed on <https://data.meereisportal.de>, and the Snow Buoy 2019S94 is published on PANGAEA (Nicolaus et al., 2020, <https://dx.doi.org/10.1594/PANGAEA.925325>).

Supplemental file

The supplemental files for this article can be found as follows:

Figure S1. Docx

Acknowledgments

This work was carried out, and data used in this manuscript were produced as part of the international Multidisciplinary drifting Observatory for the Study of the Arctic Climate (MOSAiC) with the tag MOSAiC20192020. We thank all persons involved in the expedition of the research vessel *Polarstern* during MOSAiC in 2019–2020 (AWI_PS122_00) as listed in Nixdorf et al. (2021). We highly acknowledge the contribution by Ilkka Matero, Julia Regnery, Jan Rohde, Jakob Belter, Steven Fons, Igor Sheikin, Alexey Niubom, and David Clemens-Sewall for deploying and/or recovering the radiation stations.

Funding

This work was funded by the German Federal Ministry of Education and Research (BMBF) through financing the Alfred-Wegener-Institut Helmholtz-Zentrum für Polar- und Meeresforschung (AWI) and the *Polarstern* expedition PS122 under the grant N-2014-H-060_Dethloff, the AWI through its projects: AWI_ROV, AWI_ICE, and AWI_SNOW. The AWI buoy program was funded by the Helmholtz strategic investment Frontiers in Arctic Marine Monitoring (FRAM). Part of the funding for this project was provided by the Deutsche Forschungsgemeinschaft (DFG, German Research Foundation)—Project-ID 268020496—through the Transregional Collaborative Research Centre TRR-172 “Arctic Amplification: Climate Relevant Atmospheric and Surface Processes, and Feedback Mechanisms (AC)³.” RT was funded by the Deutsche Forschungsgemeinschaft (DFG, German Research Foundation)—Project-ID

268020496—through the Transregional Collaborative Research Centre TRR-172 “Arctic Amplification: Climate Relevant Atmospheric and Surface Processes, and Feedback Mechanisms (AC)³.” PA was funded through the Alfred-Wegener-Institutes internal project AWI_ROV, through the German Ministry of Education and Research (BMBF) project MOSAiC 3—IceScan (03F0916A), and additional funds through the project DiatomARCTIC (03F0810A), part of the Changing Arctic Ocean Program, jointly funded by the UKRI Natural Environment Research Council (NERC) and the BMBF.

Competing interests

The authors have no competing interests to declare.

Author contributions

Contributed to conception and design: RT, MN, CK, CH.

Contributed to acquisition of data: MN, CK, PA, MH, GS.

Contributed to analysis and interpretation of data: RT, MN, CK, CH, EJ, MW, HN.

Drafted and/or revised the article: RT, MN, CK, CH, GS, PA, MW, EJ, HN.

Approved the submitted version for publication: All authors.

References

- Anderson, GP, Clough, SA, Kneizys, FX, Chetwynd, JH, Shettle, E.** 1986. AFGL atmospheric constituent profiles (0–120 km). Bedford, MA: Air Force Geophysical Laboratory, Hanscom Air Force Base. Technical Report AFGL-TR-86-0110.
- Anderson, M, Bliss, AC, Drobot, S.** 2019. Snow Melt Onset Over Arctic Sea Ice From SMMR and SSM/I-SSMIS Brightness Temperatures, Version 4 [dataset]. Boulder, CO: NASA National Snow and Ice Data Center Distributed Active Archive Center. DOI: <http://dx.doi.org/10.5067/A9YK15H5EBHK>. Accessed March 1, 2024.
- Ardyna, M, Mundy, CJ, Mayot, N, Matthes, L, Oziel, L, Horvat, C, Leu, E, Assmy, P, Hill, V, Matrai, PA, Gale, MA, Melnikov, IA, Arrigo, KR.** 2020. Under-ice phytoplankton blooms: Shedding light on the “invisible” part of Arctic primary production. *Frontiers in Marine Science* **7**. DOI: <http://dx.doi.org/10.3389/fmars.2020.608032>.
- Arndt, S, Nicolaus, M.** 2014. Seasonal cycle and long-term trend of solar energy fluxes through Arctic sea ice. *The Cryosphere* **8**(6): 2219–2233. DOI: <http://dx.doi.org/10.5194/tc-8-2219-2014>.
- Comiso, JC.** 2012. Large decadal decline of the Arctic multiyear ice cover. *Journal of Climate* **25**(4): 1176–1193. DOI: <http://dx.doi.org/10.1175/jcli-d-11-00113.1>.
- Ehn, JK, Mundy, CJ, Barber, DG.** 2008. Bio-optical and structural properties inferred from irradiance measurements within the bottommost layers in an Arctic landfast sea ice cover. *Journal of Geophysical Research* **113**(C3). DOI: <http://dx.doi.org/10.1029/2007jc004194>.
- Emde, C, Buras-Schnell, R, Kylling, A, Mayer, B, Gasteiger, J, Hamann, U, Kylling, JI, Richter, B, Pause, C, Dowling, TE, Bugliaro, L.** 2016. The libRadtran software package for radiative transfer calculations (version 2.0.1). *Geoscientific Model Development* **9**(5): 1647–1672. DOI: <http://dx.doi.org/10.5194/gmd-9-1647-2016>.
- Gueymard, CA.** 2004. The sun's total and spectral irradiance for solar energy applications and solar radiation models. *Solar Energy* **76**(4): 423–453. DOI: <http://dx.doi.org/10.1016/j.solener.2003.08.039>.
- Haas, C, Pfaffling, A, Hendricks, S, Rabenstein, L, Etienne, J-L, Rigor, I.** 2008. Reduced ice thickness in Arctic transpolar drift favors rapid ice retreat. *Geophysical Research Letters* **35**(17). DOI: <http://dx.doi.org/10.1029/2008gl034457>.
- Katlein, C, Arndt, S, Belter, HJ, Castellani, G, Nicolaus, M.** 2019. Seasonal evolution of light transmission distributions through Arctic sea ice. *Journal of Geophysical Research: Oceans* **124**(8): 5418–5435. DOI: <http://dx.doi.org/10.1029/2018jc014833>.
- Knust, R.** 2017. Polar Research and Supply Vessel POLARSTERN operated by the Alfred-Wegener-Institute. *Journal of Large-Scale Research Facilities JLSRF* **3**: A119. DOI: <http://dx.doi.org/10.17815/jlsrf-3-163>.
- Krumpen, T, Birrien, F, Kauker, F, Rackow, T, von Albedyll, L, Angelopoulos, M, Belter, HJ, Bessonov, V, Damm, E, Dethloff, K, Haapala, J, Haas, C, Harris, C, Hendricks, S, Hoelemann, J, Hoppmann, M, Kaleschke, L, Karcher, M, Kolabutin, N, Lei, R, Lenz, J, Morgenstern, A, Nicolaus, M, Nixdorf, U, Petrovsky, T, Rabe, B, Rabenstein, L, Rex, M, Ricker, R, Rohde, J, Shimanchuk, E, Singha, S, Smolyanitsky, V, Sokolov, V, Stanton, T, Timofeeva, A, Tsamados, M, Watkins, D.** 2020. The MOSAiC ice floe: Sediment-laden survivor from the Siberian shelf. *The Cryosphere* **14**(7): 2173–2187. DOI: <http://dx.doi.org/10.5194/tc-14-2173-2020>.
- Krumpen, T, von Albedyll, L, Goessling, H, Hendricks, S, Juhls, B, Spreen, G, Willmes, S, Belter, HJ, Dethloff, K, Haas, C, Kaleschke, L, Katlein, C, Tian-Kunze, X, Ricker, R, Rostosky, P, Rückert, JE, Singha, S, Sokolova, J.** 2021. MOSAiC drift expedition from October 2019 to July 2020: Sea ice conditions from space and comparison with previous years. *The Cryosphere* **15**(8): 3897–3920. DOI: <http://dx.doi.org/10.5194/tc-15-3897-2021>.
- Kwok, R.** 2018. Arctic sea ice thickness, volume, and multiyear ice coverage: Losses and coupled variability (1958–2018). *Environmental Research Letters* **13**(10): 105005. DOI: <http://dx.doi.org/10.1088/1748-9326/aae3ec>.
- Light, B, Smith, MM, Perovich, DK, Webster, M, Holland, MM, Linhardt, F, Raphael, I, Clemens-Sewall, D, Macfarlane, AR, Anhaus, P, Bailey, DA.** 2022. Arctic sea ice albedo: Spectral composition, spatial heterogeneity, and temporal evolution observed during the MOSAiC drift. *Elementa: Science of the Anthropocene* **10**(1). DOI: <https://doi.org/10.1525/elementa.2021.000103>.

- Lund-Hansen, LC, Markager, S, Hancke, K, Stratmann, T, Rysgaard, S, Ramløv, H, Sorrell, BK.** 2015. Effects of sea-ice light attenuation and CDOM absorption in the water below the Eurasian sector of central Arctic Ocean (>88°N). *Polar Research* **34**(1): 23978. DOI: <http://dx.doi.org/10.3402/polar.v34.23978>.
- Maslanik, JA, Stroeve, J, Fowler, CW, Emery, WJ.** 2011. Distribution and trends in Arctic sea ice age through spring 2011. *Geophysical Research Letters* **38**(13). DOI: <http://dx.doi.org/10.1029/2011gl047735>.
- Maturilli, M, Holdridge, DJ, Dahlke, S, Graeser, J, Sommerfeld, A, Jaiser, R, Deckelmann, H, Schulz, A.** 2021. Initial Radiosonde Data From 2019-10 to 2020-09 During Project MOSAiC [dataset]. Bremerhaven, Germany: Alfred Wegener Institute, Helmholtz Centre for Polar and Marine Research, PANGAEA. DOI: <http://dx.doi.org/10.1594/pangaea.928656>.
- Mayer, B, Kylling, A.** 2005. Technical note: The libRadtran software package for radiative transfer calculations—Description and examples of use. *Atmospheric Chemistry and Physics* **5**(7): 1855–1877. DOI: <http://dx.doi.org/10.5194/acp-5-1855-2005>.
- Nicolaus, M, Gerland, S, Hudson, SR, Hanson, SG, Haapala, J, Perovich, DK.** 2010a. Seasonality of spectral albedo and transmittance as observed in the Arctic transpolar drift in 2007. *Journal of Geophysical Research* **115**(C11). DOI: <http://dx.doi.org/10.1029/2009jc006074>.
- Nicolaus, M, Hoppmann, M, Lei, R, Belter, HJ, Fang, Y, Rohde, J.** 2020. Snow Height on Sea Ice, Meteorological Conditions and Drift of Sea ice From Autonomous Measurements From Buoy 2019S94, Deployed During MOSAiC 2019/20 [dataset]. Bremerhaven, Germany: Alfred Wegener Institute, Helmholtz Centre for Polar and Marine Research, PANGAEA. DOI: <http://dx.doi.org/10.1594/pangaea.925325>.
- Nicolaus, M, Hudson, SR, Gerland, S, Munderloh, K.** 2010b. A modern concept for autonomous and continuous measurements of spectral albedo and transmittance of sea ice. *Cold Regions Science and Technology* **62**(1): 14–28. DOI: <http://dx.doi.org/10.1016/j.coldregions.2010.03.001>.
- Nicolaus, M, Katlein, C, Maslanik, JA, Hendricks, S.** 2012. Changes in Arctic sea ice result in increasing light transmittance and absorption. *Geophysical Research Letters* **39**(24). DOI: <http://dx.doi.org/10.1029/2012gl053738>.
- Nicolaus, M, Perovich, DK, Spreen, G, Granskog, MA, von Albedyll, L, Angelopoulos, M, Anhaus, P, Arndt, S, Belter, HJ, Bessonov, V, Birnbaum, G, Brauchle, J, Calmer, R, Cardellach, E, Cheng, B, Clemens-Sewall, D, Dadic, R, Damm, E, de Boer, G, Demir, O, Dethloff, K, Divine, D, Fong, AA, Fons, S, Frey, MM, Fuchs, N, Gabarró, C, Gerland, S, Goessling, H, Gradinger, R, Haapala, J, Haas, C, Hamilton, J, Hannula, H-R, Hendricks, S, Herber, A, Heuzé, C, Hoppmann, M, Høyland, KV, Huntemann, M, Hutchings, JK, Hwang, B, Itkin, P, Jacobi, HW, Jaggi, M, Jutila, A, Kaleschke, L, Katlein, C, Kolabutin, N, Krampe, D, Kristensen, SS, Krumpen, T, Kurtz, NT, Lampert, A, Lange, B, Lei, R, Light, B, Linhardt, F, Liston, GE, Loose, B, Macfarlane, AR, Mahmud, M, Matero, I, Maus, S, Morgenstern, A, Naderpour, R, Nandan, V, Niubom, A, Oggier, M, Oppelt, N, Pätzold, F, Perron, C, Petrovsky, T, Pirazzini, R, Polashenski, C, Rabe, B, Raphael, I, Regnery, J, Rex, M, Ricker, R, Riemann-Campe, K, Rinke, A, Rohde, J, Salganik, E, Scharien, RK, Schiller, M, Schneebeil, M, Semmling, M, Shimanchuk, E, Shupe, MD, Smith, M, Smolyanitsky, V, Sokolov, V, Stanton, T, Stroeve, J, Thielke, L, Timofeeva, A, Tonboe, R, Tavri, A, Tsamados, M, Wagner, DN, Watkins, D, Webster, M, Wendisch, M.** 2022. Overview of the MOSAiC expedition: Snow and sea ice. *Elementa: Science of the Anthropocene* **10**(1): 000046. DOI: <http://dx.doi.org/10.1525/elementa.2021.000046>.
- Nixdorf, U, Dethloff, K, Rex, M, Shupe, M, Sommerfeld, A, Perovich, D, Nicolaus, M, Heuzé, C, Rabe, B, Loose, B, Damm, E, Gradinger, R, Fong, A, Maslowski, W, Rinke, A, Kwok, R, Spreen, G, Wendisch, M, Herber, A, Hirsekorn, M, Mohaupt, V, Frickenhaus, S, Immerz, A, Weiss-Tuider, K, König, B, Mergedoh, D, Regnery, J, Gerchow, P, Ransby, D, Krumpen, T, Morgenstern, A, Haas, C, Kanzow, T, Rack, FR, Saitzev, V, Sokolov, V, Makarov, A, Schwarze, S, Wunderlich, T, Wurr, K, Boetius, A.** 2021. MOSAiC extended acknowledgement. Zenodo. DOI: <https://doi.org/10.5281/zenodo.5541624>.
- Perovich, DK.** 2005. On the aggregate-scale partitioning of solar radiation in Arctic sea ice during the Surface Heat Budget of the Arctic Ocean (SHEBA) field experiment. *Journal of Geophysical Research* **110**(C3). DOI: <http://dx.doi.org/10.1029/2004jc002512>.
- Perovich, DK, Cota, GF, Maykut, GA, Grenfell, TC.** 1993. Bio-optical observations of first-year Arctic sea ice. *Geophysical Research Letters* **20**(11): 1059–1062. DOI: <http://dx.doi.org/10.1029/93gl01316>.
- Perovich, DK, Elder, B.** 2002. Estimates of ocean heat flux at SHEBA. *Geophysical Research Letters* **29**(9): 58-1–58-4. DOI: <http://dx.doi.org/10.1029/2001gl014171>.
- Perovich, DK, Polashenski, C.** 2012. Albedo evolution of seasonal Arctic sea ice. *Geophysical Research Letters* **39**(8). DOI: <http://dx.doi.org/10.1029/2012gl051432>.
- Perovich, DK, Richter-Menge, JA.** 2015. Regional variability in sea ice melt in a changing Arctic. *Philosophical Transactions of the Royal Society A* **373**(2045): 20140165. DOI: <http://dx.doi.org/10.1098/rsta.2014.0165>.
- Perovich, DK, Richter-Menge, JA, Jones, KF, Light, B.** 2008. Sunlight, water, and ice: Extreme Arctic sea ice melt during the summer of 2007. *Geophysical Research Letters* **35**(11). DOI: <http://dx.doi.org/10.1029/2008gl034007>.
- Perovich, DK, Roesler, CS, Pegau, WS.** 1998. Variability in Arctic sea ice optical properties. *Journal of*

- Geophysical Research* **103**(C1): 1193–1208. DOI: <http://dx.doi.org/10.1029/97jc01614>.
- Serreze, MC, Stroeve, J.** 2015. Arctic sea ice trends, variability and implications for seasonal ice forecasting. *Philosophical Transactions of the Royal Society A* **373**(2045): 20140159. DOI: <http://dx.doi.org/10.1098/rsta.2014.0159>.
- Smith, RC, Baker, KS.** 1981. Optical properties of the clearest natural waters (200–800 nm). *Applied Optics* **20**(2): 177–184. DOI: <http://dx.doi.org/10.1364/ao.20.000177>.
- Stamnes, K, Tsay, SC, Wiscombe, W, Laszlo, I.** 2000. DISORT, a general-purpose Fortran program for discrete-ordinate-method radiative transfer in scattering and emitting layered media: Documentation of methodology. Technical report.
- Stroeve, J, Markus, T, Boisvert, LN, Miller, JA, Barrett, AP.** 2014. Changes in Arctic melt season and implications for sea ice loss. *Geophysical Research Letters* **41**(4): 1216–1225. DOI: <http://dx.doi.org/10.1002/2013gl058951>.
- Stroeve, J, Notz, D.** 2018. Changing state of Arctic sea ice across all seasons. *Environmental Research Letters* **13**(10): 103001. DOI: <http://dx.doi.org/10.1088/1748-9326/aade56>.
- Tao, R, Anhaus, P, Arndt, S, Belter, HJ, Hoppmann, M, Katlein, C, Matero, I, Regnery, J, Rohde, J, Nicolaus, M.** 2023. Spectral radiation fluxes, albedo and transmittance from autonomous measurements, deployed during MOSAiC 2019/20. Bremerhaven, Germany: Alfred Wegener Institute, Helmholtz Centre for Polar and Marine Research, PANGAEA. DOI: <https://doi.pangaea.de/10.1594/PANGAEA.949556>. Accessed April 25, 2024.
- Thielke, L, Fuchs, N, Spreen, G, Tremblay, B, Birnbaum, G, Huntemann, M, Hutter, N, Itkin, P, Jutila, A, Webster, MA.** 2023. Preconditioning of summer melt ponds from winter sea ice surface temperature. *Geophysical Research Letters* **50**(4): e2022GL101493. DOI: <http://dx.doi.org/10.1029/2022gl101493>.
- Webster, M, Holland, MM, Wright, N, Hendricks, S, Hutter, N, Itkin, P, Light, B, Linhardt, F, Perovich, DK, Raphael, I, Smith, M, von Albedyll, L, Zhang, J.** 2022. Spatiotemporal evolution of melt ponds on Arctic sea ice: MOSAiC observations and model results. *Elementa: Science of the Anthropocene* **10**(1): 000072. DOI: <http://dx.doi.org/10.1525/elementa.2021.000072>.
- Wendisch, M, Brückner, M, Crewell, S, Ehrlich, A, Notholt, J, Lüpkes, C, Macke, A, Burrows, JP, Rinke, A, Quaas, J, Maturilli, M, Schemann, V, Shupe, MD, Akansu, EF, Velasco, CB, Bärfuss, K, Blechschmidt, AM, Block, K, Bougoudis, I, Bozem, H, Böckmann, C, Bracher, A, Bresson, H, Bretschneider, L, Buschmann, M, Chechin, D, Chylik, J, Dahlke, S, Deneke, H, Dethloff, K, Donth, T, Dorn, W, Dupuy, R, Ebell, K, Egerer, U, Engelmann, R, Eppers, O, Gerdes, R, Gierens, R, Gorodetskaya, I, Gottschalk, M, Griesche, H, Gryanik, VM, Handorf, D, Harm-Altstädter, B, Hartmann, J, Hartmann, M, Heinold, B, Herber, A, Herrmann, H, Heygster, G, Höschel, I, Hofmann, Z, Hölemann, J, Hünenbein, A, Jafariserajehlou, S, Jäkel, E, Jacobi, C, Janout, M, Jansen, F, Jourdan, O, Jurányi, Z, Kalesse-Los, H, Kanzow, T, Käthner, R, Kliesch, LL, Klingebiel, M, Knudsen, EM, Kovács, T, Körtke, W, Krampe, D, Kretzschmar, J, Kreyling, D, Kulla, BS, Kunkel, D, Lampert, A, Lauer, M, Lelli, L, von Lerber, A, Linke, O, Löhnert, U, Lonardi, M, Losa, SN, Losch, M, Maahn, M, Mech, M, Mei, L, Mertes, S, Metzner, EP, Mewes, D, Michaelis, J, Mioche, G, Moser, M, Nakoudi, K, Neggens, R, Neuber, R, Nomokouva, T, Oelker, J, Papakonstantinou-Presvelou, I, Pätzold, F, Pefanis, V, Pohl, C, van Pinxteren, M, Radovan, A, Rhein, M, Rex, M, Richter, A, Risse, N, Ritter, C, Rostosky, P, Rozanov, VV, Ruiz Donoso, E, Saavedra-Garfias, P, Salzmann, M, Schacht, J, Schäfer, M, Schneider, JM, Schnierstein, N, Seifert, P, Seo, S, Siebert, H, Soppa, MA, Spreen, G, Stachlewska, IS, Stapf, J, Stratmann, F, Tegen, I, Viceto, C, Voigt, C, Vountas, M, Walbröl, A, Walter, M, Wehner, B, Wex, H, Willmes, S, Zanatta, M, Zeppenfeld, S.** 2023. Atmospheric and surface processes, and feedback mechanisms determining arctic amplification: A review of first results and prospects of the (AC)³ project. *Bulletin of the American Meteorological Society* **104**(1): E208–E242. DOI: <http://dx.doi.org/10.1175/bams-d-21-0218.1>.
- Woźniak, B, Dera, J.** 2007. *Light absorption in sea water*. New York, NY: Springer eBooks. DOI: <http://dx.doi.org/10.1007/978-0-387-49560-6>.

How to cite this article: Tao, R, Nicolaus, M, Katlein, C, Anhaus, P, Hoppmann, M, Spreen, G, Niehaus, H, Jäkel, E, Wendisch, M, Haas, C. 2024. Seasonality of spectral radiative fluxes and optical properties of Arctic sea ice during the spring–summer transition. *Elementa: Science of the Anthropocene* 12(1). DOI: <https://doi.org/10.1525/elementa.2023.00130>

Domain Editor-in-Chief: Jody W. Deming, University of Washington, Seattle, WA, USA

Associate Editor: Stephen F. Ackley, Department of Geological Sciences, University of Texas at San Antonio, TX, USA

Knowledge Domain: Ocean Science

Part of an Elementa Special Feature: The Multidisciplinary Drifting Observatory for the Study of Arctic Climate (MOSAIC)

Published: May 09, 2024 **Accepted:** March 18, 2024 **Submitted:** November 06, 2023

Copyright: © 2024 The Author(s). This is an open-access article distributed under the terms of the Creative Commons Attribution 4.0 International License (CC-BY 4.0), which permits unrestricted use, distribution, and reproduction in any medium, provided the original author and source are credited. See <http://creativecommons.org/licenses/by/4.0/>.



Elem Sci Anth is a peer-reviewed open access journal published by University of California Press.

OPEN ACCESS The Open Access logo, consisting of the words 'OPEN ACCESS' followed by a circular icon containing a stylized padlock with an open keyhole.